ACS Catalysis
Research Article
pubs.acs.org/acscatalysis

Yolk−Satellite−Shell Structured Ni−Yolk@Ni@SiO_2 Nanocomposite: Superb Catalyst toward Methane CO_2 Reforming Reaction

Ziwei Li, Liuye Mo, Yasotha Kathiraser, and Sibudjing Kawi*

Department of Chemical and Biomolecular Engineering, National University of Singapore, Singapore 119260, Republic of Singapore

S *Supporting Information*

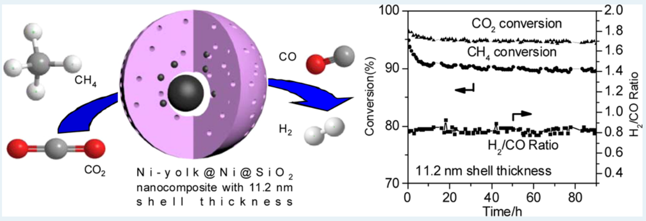

ABSTRACT: The CO_2 (dry) reforming of methane (DRM) reaction is an environmentally benign process to convert two major greenhouse gases into synthesis gas for chemical and fuel production. A great challenge for this process involves developing catalysts with high carbon resistance abilities. Herein we synthesize, for the first time, a yolk−satellite−shell structured Ni−yolk@Ni@SiO_2 nanocomposite for the DRM reaction by varying the shell thickness of Ni@SiO_2 core shell nanoparticles. The formation of Ni−yolk@Ni@SiO_2 is proved to be shell thickness dependent. Compared with Ni@SiO_2, Ni−yolk@Ni@SiO_2 with 11.2 nm silica shell thickness shows stable and near equilibrium conversion for CH_4 and CO_2 for 90 h at 800 °C with negligible carbon deposition. The dual effects of formation of small satellite Ni particles due to strong Ni−SiO_2 interactions and yolk shell structures contribute to its high activity and stability. These findings shed light on the design of other metal yolk silica shell nanocomposites to be utilized in renewable energy transfer processes such as DRM reactions driven by solar energy.

KEYWORDS: *Ni−yolk@Ni@SiO_2, satellite Ni, nanocomposite, superb catalyst, methane CO_2 reforming*

1. INTRODUCTION

As one of the major technologies to produce clean and efficient energy, the CO_2 (dry) reforming of methane reaction (DRM) has attracted increasing attention. It mitigates the emission of notorious global warming gases (CO_2 and methane) while producing the energy carrier synthesis gas with a moderate hydrogen-to-carbon monoxide ratio, which has a higher energy efficiency to be preferentially used for the production of easier transportable liquid fuel energies such as methanol, light olefins and gasoline.[1] In addition, its endothermic property makes DRM a promising method for energy storage and energy transfer, for example, from solar energy to chemical energy, which is referred to as solar reforming of CO_2 with methane and has been studied for more than two decades.[2−6] For the DRM reaction to be driven by renewable energy sources such as solar energy, major issues that need to be addressed are high temperature (typically 700 to 860 °C) catalyst stability and performance. As for the stability problem, severe carbon deposition on the cheap Ni metal based catalysts proved to be the main issue, which hinders the industrial progress of the DRM reaction.[7]

Numerous efforts have been made to relieve this problem by preventing the sintering of Ni because it has been demonstrated that Ni particle size has a profound influence on coke resistance.[8−12] These methods include preparing highly dispersed Ni/NiM (M = Cu, Ru and Ce) bimetallics supported on metal oxide catalysts,[13−16] modifying the properties of support such as doping with basic alkaline and rare earth metals,[14,17] as well as designing catalysts with certain structures like perovskite,[17,18] spinel[19] and solid solutions.[20,21] In addition, cerium supported catalysts also received great attention because of their redox property and oxygen mobility to minimize carbon deposition.[22−24] These methods successfully prepared catalysts with good dispersion of Ni metal and high carbon resistance. Recently, another method-embedding active metal phase in inorganic cavities shows promising application in preventing sintering of active metal.[25] Among these embedded materials, metal/bimetal@oxide core shell structure nanoparticles have been demonstrated to have good properties in various applications, for example, Ni@SiO_2[26] and NiCo@SiO_2[27] for partial oxidation of methane reactions, NiPt@SiO_2[28] as magnetic materials, Ni@Al_2O_3 and Ni@MgO for NH_3 decomposition reactions[29] and Pd@CeO_2/Al_2O_3[30] for methane combustion reactions. Of particular interest is Ni@SiO_2 core shell system. This is because it has great potential to be developed as commercial catalyst due to its ease of preparation and low cost. In addition, its structure is easy to be modified such as its porosity through modification of silica shell to further improve its catalytic performance. In fact, Ni@SiO_2 has been widely applied in many fields such as chemosensors and adsorbents,[31] magnetic devices[32,33] and especially in catalytic reactions such as methane partial oxidation,[26,34] steam reforming with methane,[35] steam reforming with propane,[36] hydrogen transfer of ketones[37] and 4-nitrophenol reduction reactions.[38] They turned out to be good catalysts with high activity and stability as well as low carbon deposition because

Received: November 5, 2013
Revised: January 30, 2014
Published: March 21, 2014

dx.doi.org/10.1021/cs401027p | *ACS Catal.* 2014, 4, 1526−1536

Scheme 1. Schematic Illustration of the Formation Process of Ni−yolk@Ni@SiO_2 Nanocomposite

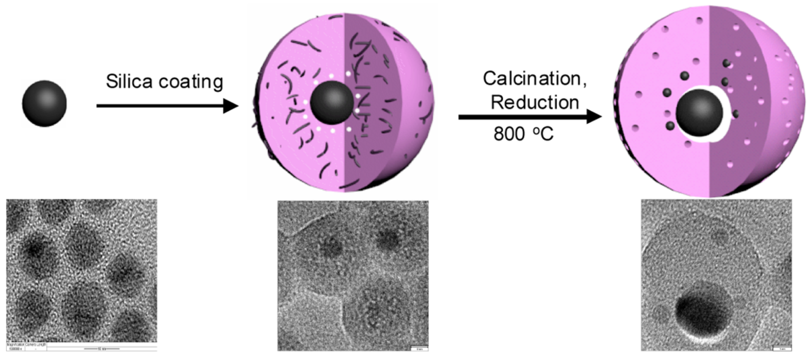

Ni nanoparticle

Ni@SiO_2 core shell nanoparticle with surfactants (gray curves) and preferentially generated pores (white color) in the inner core part

Ni-yolk@Ni@SiO_2 nanocomposite

the silica shell plays an important role in limiting the particle size of metal core even at temperature as high as 750 °C.[26,34−36,39−41] Therefore, it is expected that when Ni@SiO_2 core shell nanoparticles are used for the DRM reaction, they certainly will show good carbon resistance. However, in this study, we find that even with the protection of the silica shell, Ni@SiO_2 nanoparticles do not always have good catalytic activity with low carbon deposition for the DRM reaction.

Present studies on metal@silica core shell nanoparticles including Ni@SiO_2 in catalytic fields have been mainly focused on the metal core being the effect of different particle sizes,[26,35] the composition of bimetallic core@silica shell structure,[27,42] the cavity between the metal core and silica shell, which is the so-called yolk shell structure,[43] as well as the shell porosity.[44] All these factors have great impacts on catalytic performance in that they have a direct influence to the catalytic active metal. The effect of the silica shell thickness of core shell nanoparticles as catalysts has seldom been reported.

Herein, by combining the advantages of yolk shell structure and high activity and carbon resistant ability of smaller Ni particle sizes, we synthesize, for the first time, a yolk−satellite−shell structured Ni−yolk@Ni@SiO_2 nanocomposite as a catalyst for the DRM reaction. Our focus has been to tackle the carbon deposition problem while maintaining high catalytic activity and stability. The formation of Ni−yolk@Ni@SiO_2 is silica shell thickness dependent. With increases in shell thickness, Ni@SiO_2 structural stability for the DRM reaction greatly improves enhancing carbon resistance ability. When silica shell thickness increased to 11.2 nm, Ni−yolk@Ni@SiO_2 formed. Sintering resistant small satellite Ni particles around the Ni core within the silica shell, which was formed by decomposition of nickel phyllosilicate species at the Ni silica interface upon reduction, results in high catalytic activity (Scheme 1). The yolk shell structure transformation with the increase of shell thickness through simple calcination process further improves the catalytic activity (Scheme 1). These combined effects yield the superior catalytic performance of the Ni−yolk@Ni@SiO_2 catalyst for the DRM reaction at high temperature, which is promising for use in sustainable energy processes such as the DRM reaction driven by solar energy.

2. RESULTS AND DISCUSSION

2.1. Synthesis and Morphology of Ni−yolk@Ni@SiO_2 Nanocomposites and Ni@SiO_2 Core Shell Nanoparticles with Different Shell Thicknesses.

Detailed procedures are described in the Experimental Section. First, Ni nanoparticles with 11.7 ± 1.8 nm diameters were successfully synthesized (see Figure S1a,c, Supporting Information). The XRD pattern (Figure S1b, Supporting Information) shows the characteristic diffraction peaks of the Ni metal, corresponding to the face-centered-cubic structure of (111), (200) and (220) planes (JCPDS no. 65-2865). Second, by precisely controlling the amount of TEOS and its hydrolysis time (see Table S1, Supporting Information), Ni@SiO_2 with different shell thicknesses of 3.3 ± 2.2 nm, 5.7 ± 3.2 nm, 8.6 ± 2.5 nm, 11.2 ± 3.1 nm and 15.1 ± 2.9 nm were successfully synthesized based on their relative size to the 11.7 nm Ni metal core (see Figures 1A−E,a−e and S2A−E, Supporting Information).

It is interesting to observe from Figure 1I−V that when shell thickness is equal to or greater than 11.2 nm, the Ni@SiO_2 core shell structure evolved into the Ni−yolk@Ni@SiO_2 nanocomposite upon calcination at 800 °C for 2 h. This means that when the particle size of Ni@SiO_2 is equal to or greater than 34 ± 4.8 nm, the core shell structure transformed into a yolk shell structure (see Figure 1IV−V). This is consistent with the transformation size range of solid SiO_2 nanospheres to hollow structures reported by Sang-Jae Park.[45]

On the basis of the formation mechanism of hollow SiO_2 nanoparticles, the structural evolution of Ni@SiO_2 core shell nanoparticles can be interpreted as follows: for Ni@SiO_2 smaller than 28.9 ± 3.2 nm, due to the similar surface energy of pores at the exterior shell side and in the core side, the pores generated by ammonia etching during the Ni@SiO_2 synthesis process and by surfactant removal during the calcination process will be evenly distributed within the shell. Therefore, no large obvious void was formed. While for Ni@SiO_2 greater than 34 ± 4.8 nm, the surface energy of the pores in the core part is higher than that at the exterior shell part. Consequently, the newly generated pores by ammonia etching will preferentially grow and merge with the previous pores in the core side to reduce their surface energy. In addition, the core part of Ni@SiO_2 is less dense and more porous than the exterior shell part (see Figure 1d,e). This can be attributed to the fact that the formation process of solid SiO_2 and silica shell of Ni@SiO_2 is similar: TEOS hydrolysis followed by silica monomer addition. The preferential pore growth and mergence in the core part of Ni@SiO_2 is facilitated by calcination. It

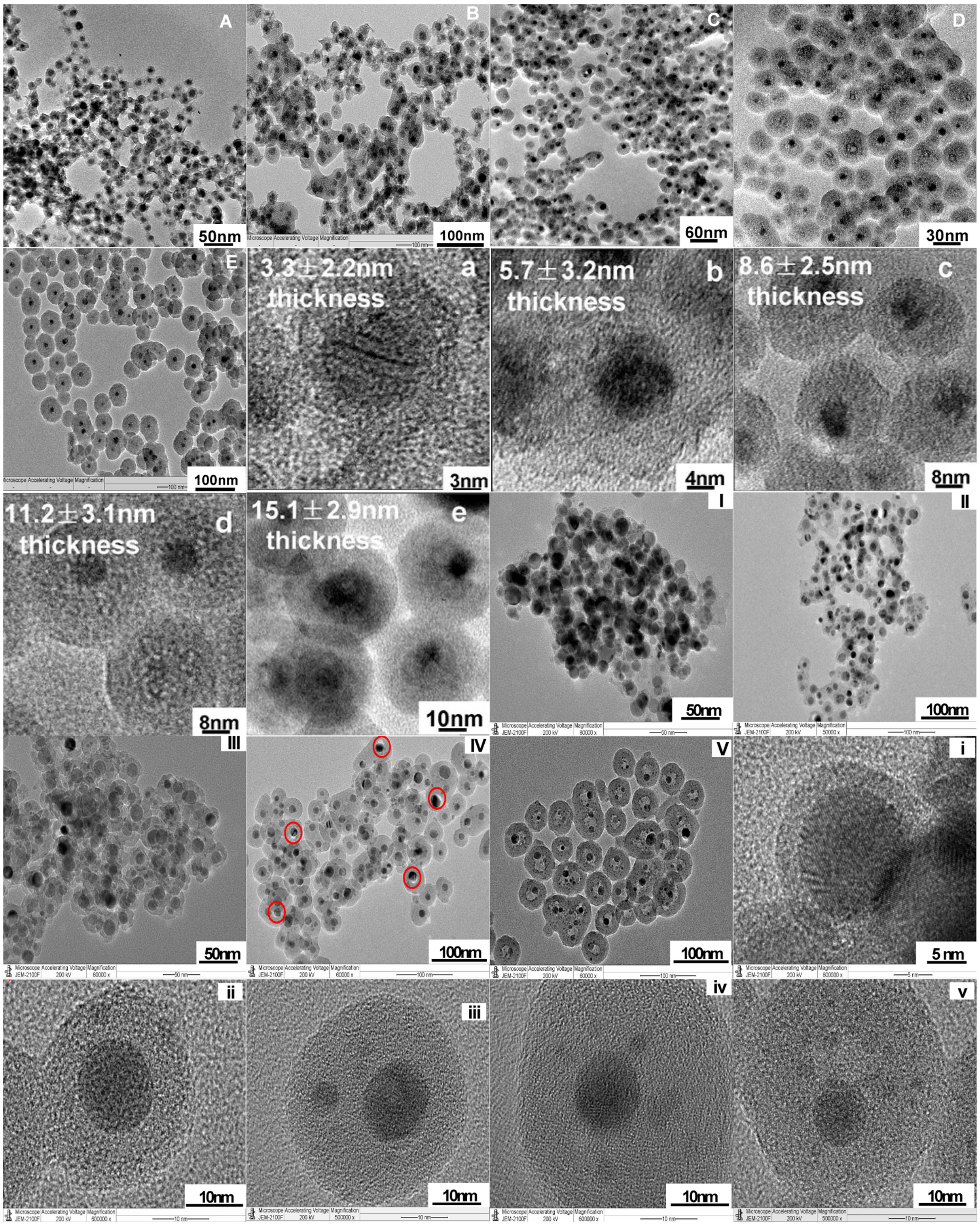

Figure 1. TEM images of Ni@SiO$_2$ and Ni−yolk@Ni@SiO$_2$ with different shell thicknesses: (A−E) as synthesized, (a−e) high magnification for as synthesized samples, (I−V) after reduction under H$_2$ at 800 °C for 2 h and (i−v) high magnification for reduced samples.

promotes this merging process by generating newer pores due to surfactant removal.

The formation of satellite Ni within SiO$_2$ shell will be discussed and characterized below.

2.2. Catalytic Activity and Stability Test. To get the intrinsic activity data and TOF (turn over frequency) data, reaction conditions should be determined to exclude the external and internal mass transfer limitation. DRM reactions at 800 °C under three different testing conditions[46] using a 3.3 nm shell thickness for Ni@SiO$_2$ and a 12.1 nm shell thickness for Ni−yolk@Ni@SiO$_2$ as examples were done as shown in Figure S3 (Supporting Information). It can be seen from Figure S3 (Supporting Information) that the deviations of CO$_2$ and CH$_4$ conversions under all the three testing conditions are less than 10%. This indicates that both external and internal mass transfer limitations were excluded under the testing GHSV value of 1440 L·g^{-1} cat·h^{-1}. To compare the activity of these catalysts, the same GHSV value of 1440 L·g^{-1} cat·h^{-1} and same catalyst amount (0.01 g) were used. Considering that Ni loading is different among these catalysts (Table S1, Supporting Information), the activity (Figure 2) was expressed as specific activity (expressed in terms of mol of CO_2 or CH_4 converted per mol of total Ni per minute) based on the same Nickel content. From Figure 2a, it can be clearly seen that a small increase in shell thickness from 3.3 to 5.7 nm resulted in a nearly doubled increase in CH_4 specific activity (from 0.058 to 0.112 mol·mol^{-1}(Ni)·min^{-1} at 20 h) and a tripled increase in CO_2 specific activity (from 0.053 to 0.163 mol·mol^{-1}(Ni)·min^{-1} at 20 h) (see Figure 2a). Even though further increases in shell thickness to 8.6 nm did not bring about a significant increase of specific activity, CH_4 specific activity became more stable compared with 3.3 and 5.7 nm shell thickness catalysts. The most stable and active result was obtained for the 11.2 nm shell thickness Ni−yolk@Ni@SiO$_2$ with CH_4 and CO_2 specific activities of 0.16 and 0.21 mol·mol^{-1}(Ni)·min^{-1}, respectively. However, with the continuous increases in shell thickness to 15.1 nm for Ni−yolk@Ni@SiO$_2$, a significant drop of specific activity was observed. These results obviously indicated the great influence of silica shell thickness to the catalyst structure and catalytic activity and stability.

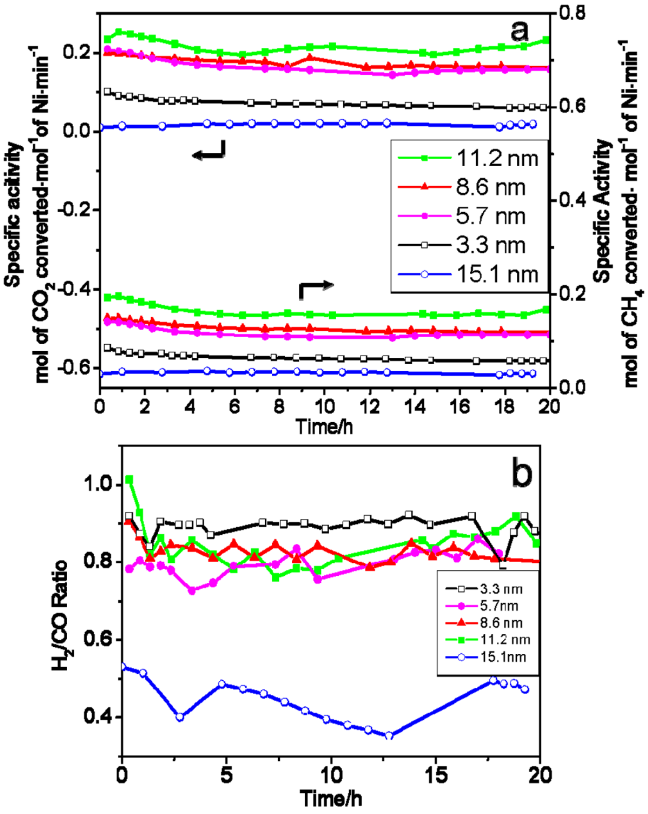

Figure 2. Specific activity and H_2/CO ratio for Ni@SiO$_2$ and Ni−yolk@Ni@SiO$_2$ with different shell thicknesses. Conditions: 800 °C, GHSV = 1440 L·g^{-1} cat·h^{-1}, W_{cat} = 0.01 g, CO_2:CH_4:N_2 = 1:1:1.

Figure 2b presents the variations of H_2/CO ratio with silica shell thickness. When shell thickness increased from 3.3 to 5.7 nm, an obvious drop from ca. 0.9 to ca. 0.8 occurred. With the continuous increase of shell thickness to 11.2 nm, a slight increase but comparable H_2/CO ratio of 0.82 was found. However, when the shell thickness reached 15.1 nm for Ni−yolk@Ni@SiO$_2$, the H_2/CO ratio suddenly dropped to ca. 0.4, which is in accordance with its low activity.

The initial TOF value of CH_4 was calculated based on the surface Ni exposure from H_2 chemisorption (see Table 1). It is difficult to compare them with other core shell catalysts because the availability of TOF value for core shell catalysts is scarce. However, when our catalysts were compared with the reported Ni surface exposure value of other core shell catalysts,[29,47] they were found to be in the same order of magnitude. In addition, the low Ni dispersion and high TOF value compared with supported Ni catalysts for the DRM reaction (see Table 1) are also consistent with the reported values of core shell catalysts for other reactions, which demonstrated the high activity of core shell catalysts due to the confinement effect.[29,47] Specifically, the initial CH_4 TOF showed a similar trend to the specific activity with the increase in shell thickness. An 11.2 nm shell thickness Ni−yolk@Ni@SiO$_2$ gave the highest initial CH_4 TOF value of 79 s^{-1}.

The most active and stable 11.2 nm shell thickness Ni−yolk@Ni@SiO$_2$ within 20 h was tested under normal conditions: GHSV value of 36 000 mL·g^{-1} cat·h^{-1} and catalyst amount of 0.05 g for 90 h (see Figure 3). As a comparison, a 3.3 nm shell thickness Ni@SiO$_2$ with the same Ni content was also tested under the same GHSV value. As can be seen from Figure 3, the 11.2 nm shell thickness Ni−yolk@Ni@SiO$_2$ showed a considerably stable and high conversion of 90% and 95% for both CH_4 and CO_2, respectively, which is near the equilibrium conversion (94% for CH_4 and 98% for CO_2 at 800 °C[48]). However, for the 3.3 nm shell thickness Ni@SiO$_2$, CH_4 and CO_2 conversions dropped by 27.6% (from 82.9% to 60%) and 14.7% (from 86.2% to 73.5%), respectively, within the 90 h of testing.

2.3. Structural Stability and Carbon Resistance Property.

Figure 4 demonstrates the morphologies of spent catalysts. Overall, great changes took place for catalyst morphologies with shell thicknesses of 3.3 and 15.1 nm (Figure 4a,e). Severe Ni sintering and carbon deposition occurred for the 3.3 nm shell thickness catalyst. While instead of Ni sintering, cross-linking between Ni−yolk@Ni@SiO$_2$'s

Table 1. Surface Ni Exposure and Initial TOF$_{CH4}$ Data Obtained from H_2 Chemisorption

thickness (nm)	Ni$_w$[a] (%)	Ni$_{sur}$[b] /μ mol·g^{-1} cat	Ni$_{Dis}$[c] (%)	conv(CH_4)[d] (%)	TOF$_{ini}$(CH_4)[e] /s^{-1}
3.3	63.5	19.92	0.184	14.1	39
5.7	39.5	10.96	0.163	13.1	65
8.6	29.5	8.40	0.167	12.0	78
11.2	18.6	6.94	0.219	10.0	79
15.1	13.8	2.9	0.123	2.0	38

[a] Ni$_w$: Ni loading determined from ICP characterization. [b] Ni$_{sur}$: Ni surface exposure measured from H_2 chemisorption. [c] Ni$_{Dis}$: Ni dispersion measured from H_2 chemisorption. [d] conv(CH_4): CH_4 conversion at first 2 h of reaction. Reaction Conditions: 800 °C, GHSV = 1440 L·g^{-1}cat·h^{-1}, W_{cat} = 0.01 g, CO_2:CH_4:N_2 = 1:1:1. [e] TOF$_{ini}$(CH_4) initial TOF value of CH_4 at first 2 h of reaction.

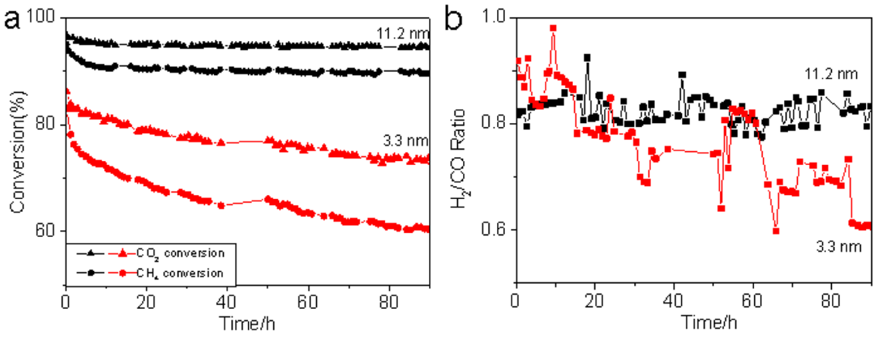

Figure 3. Stability test for Ni@SiO_2 with 3.3 nm shell thickness and Ni−yolk@Ni@SiO_2 with 11.2 nm shell thickness. Conditions: 800 °C, GHSV = 36 000 mL·g^{-1} cat·h^{-1}, CO_2:CH_4:N_2 = 1:1:1.

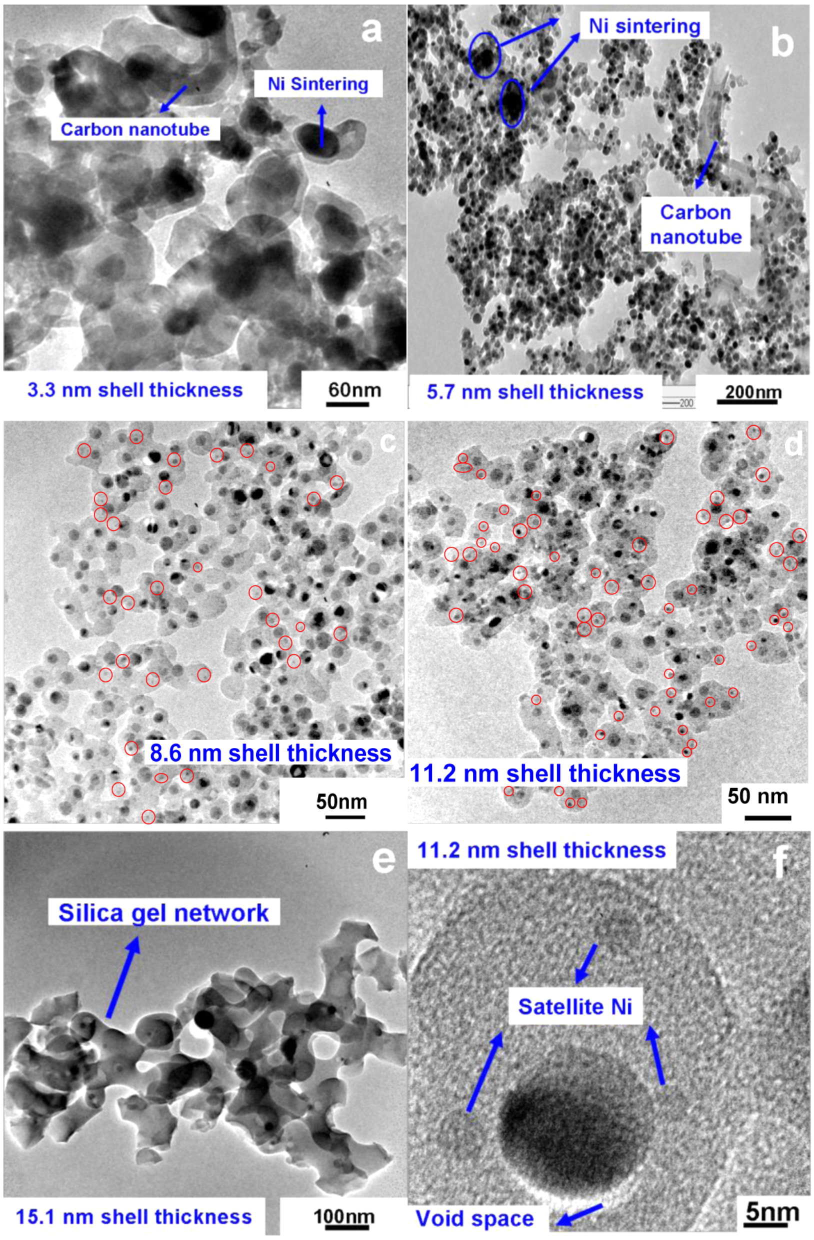

Figure 4. TEM images of spent catalysts with different shell thicknesses after 20 h of reaction: (a−e) low magnification and (f) high magnification for Ni−yolk@Ni@SiO_2 with 11.2 nm shell thickness.

with 15.1 nm shell thickness occurred. Compared with the 3.3 nm shell thickness catalyst, although the Ni sintering problem for the 5.7 nm shell thickness catalyst still exists, much improvement can be observed. Neither Ni sintering nor cross-linking between particles was observed for the 8.6 nm Ni@SiO_2 and 11.2 nm shell thickness Ni−yolk@Ni@SiO_2. In addition, small satellite Ni nanoparticles around the Ni core within the silica shell were observed (in Figure 4c,d, indicated by red circle, and Figure 4f), which was also confirmed from TPR characterization below.

Specifically, the 3.3 nm shell thickness catalyst was reconstructed with carbon encapsulated the sintered Ni, as indicated with red and green colors, respectively, in EDX mapping in Figure S4 (Supporting Information). Silica was distributed randomly in the catalyst system but not around sintered Ni. Even though it is not accurate to quantitatively analyze carbon deposition using EDX because the result may be distorted by carbon from the carbon film of the copper grid, we can clearly know the distribution of each element from it. To prove our postulation that the sintering of Ni was not caused only by long time exposure to high temperature, fresh catalyst was calcined at 800 °C for 20 h, which is same with the reaction time and examined by TEM (Figure S5a, Supporting Information). As can be seen from Figure S5a (Supporting Information), Ni did not sinter and kept the same morphology with the one calcined for 2 h. This proved that the Ni@SiO_2 catalyst with 3.3 nm shell thickness was structurally stable at 800 °C. Therefore, we can conclude that the sintering of Ni occurred during the reaction. The continuous depositing of carbon species on the Ni surface may break the very thin silica shell due to the weak Ni core and silica shell interaction for the 3.3 nm shell thickness catalyst, as proved by XPS and TPR characterizations (Figures 8 and 9). This will lead to the sintering of Ni and, therefore, more severe carbon formation around Ni was observed from Figure 4a. In addition, it is observed that even though encapsulated carbon is formed, the activity did not drop rapidly during the 20 h reaction. Reasons accounting for this will be discussed below.

As for 15.1 nm thickness Ni−yolk@Ni@SiO_2, in order to confirm that cross-linking between silica shells occurred during reaction, fresh catalysts were calcined for 20 h at 800 °C and characterized by TEM (Figure S5b, Supporting Information). Like the 3.3 nm thickness catalyst, the 15.1 nm thickness Ni−yolk@Ni@SiO_2 kept its morphology except that the particle seems to become denser due to further dehydration between hydroxyl groups. But cross-linking did not take place. Therefore, we can conclude that cross-linking happened due to water produced by reverse water gas shift reaction, which is consistent with its low H_2/CO ratio (Figure 2b). This leads to hydroxylation between −(Si−O−Si)− groups producing polymeric chains of $-Si(OH)_2-O-Si(OH)_2-OH$ groups, which link up to form three-dimensional networks.[49]

Figure 5 depicts thermogravimetric analysis (TGA) and differential thermoanalysis (DTA) characterizations for spent catalysts. The carbon resistant effect of silica shell thickness can be clearly seen from this analysis. When the shell thickness increased from 3.3 to 5.7 nm, the amount of carbon deposition decreased by 66% (Figure 5a). Negligible carbon was detected when the shell thickness was greater than 8.6 nm. The weight increase from 250 to 800 °C with maxima around 400 °C in Figure 5a can be attributed to the oxidation of Ni to NiO, corresponding to the exothermal peak centered at approximately 390 °C in Figure 5b. This is consistent with the oxidation of pure Ni powder.[50] It is worth noting that even though Ni loading for the 3.3 nm Ni@SiO_2 catalyst is the highest, the exothermic peak for Ni oxidation was not as obvious as 5.7 and 8.6 nm Ni@SiO_2 catalysts. This can probably be attributed to the coverage of Ni by carbon as can be seen from the TEM image shown in Figure 4a for the spent catalyst. This carbon coverage leads to the slow and partial oxidation of Ni. This can be verified from the TGA curve, which shows that the weight increase for the 3.3 nm Ni@SiO_2 catalyst started at even higher temperature than the 8.6 nm Ni@SiO_2 catalyst. Even though the 3.3 nm Ni@SiO_2 catalyst has the highest Ni loading, its weight increase ratio is similar to those of 8.6 or 5.7 nm Ni@SiO_2 catalysts. This further confirms that Ni could be slowly and partially oxidized before all the carbon was removed. These results could possibly explain why the exothermic Ni-oxidation peak for the 3.3 nm Ni@SiO_2 catalyst was not so obvious even though it has the highest Ni loading. The different weight increase for 8.6 nm thickness Ni@SiO_2 (8.5%) and Ni−yolk@Ni@SiO_2 with 11.2 nm thickness (4.8%) and 15.1 nm thickness (1.2%) spent catalyst can be attributed to different accessibility of Ni to oxygen after reaction. This is consistent with the Ni exposure extent determined by H_2 chemisorptions (see Table 1).

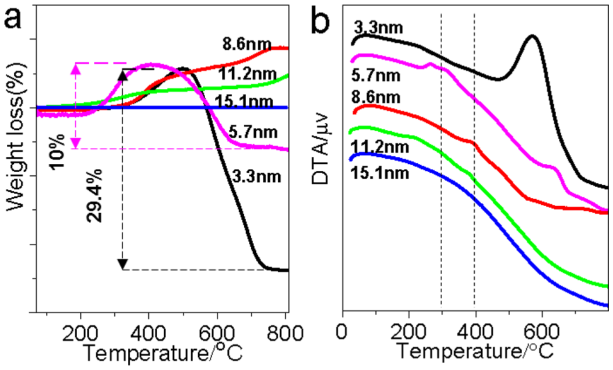

Figure 5. TGA (a) and DTA (b) patterns for spent catalysts with different shell thickness.

The weight loss from 500 to 800 °C corresponding to the exothermal peak, centered at around 590 and 680 °C in Figure 5b, is due to the oxidation of the deposited carbon. Specifically, these two exothermal peaks were assigned to α-type carbon (C_α) and β-type carbon (C_β), respectively.[51] C_α are active species for the formation of syngas while C_β are inactive species causing deactivation of the catalyst.[52] From Figure 5b, it is obvious that most of the carbon deposition is in the form of C_α. That is why even though there is 29.4% carbon deposition for the 3.3 nm shell thickness catalyst, the activity did not drop dramatically within 20 h of reaction.

2.4. Physicochemical Features. The XRD patterns of Ni@SiO_2 and Ni−yolk@Ni@SiO_2 with different shell thickness before and after calcination at 800 °C for 2 h are shown in Figure 6. Peaks located at 2θ = 44.5°, 51.8° and 76.4° (Figure 6a) can be assigned to Ni (JCPDS no. 65-2865), whereas peaks centered at 2θ = 37.1°, 43.1° and 62.6° (Figure 6b) correspond to NiO (JCPDS no. 65-2901). As revealed by Figure 6, with the increase of shell thickness, the silica peak intensity (centered at 23.5°) increases, while the Ni peak intensity decreases. Specifically, the peak areas of NiO (200) (Figure 6b) are measured to be 1040.4, 603.7, 456.9, 321.8, and 222.4, respectively, for the thicknesses of 3.3, 5.7, 8.6, 11.2 and 15.1 nm. The peak area ratio (1:1.7:2.3:3.2:4.7) is in good accordance with the NiO weight ratio (1:1.6:2.2:3.4:4.6) determined from ICP analysis (Table S1, Supporting Information). In addition, NiO peaks indicated by the star symbol in Figure 6a were observed for the 3.3 nm shell

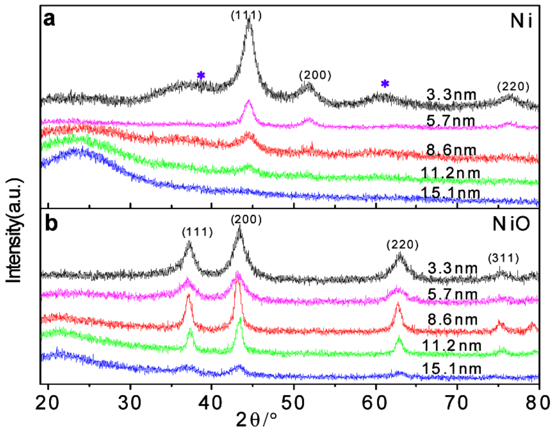

Figure 6. XRD Patterns of Ni@SiO_2 and Ni−yolk@Ni@SiO_2 with different shell thickness: (a) as synthesized and (b) after calcination at 800 °C for 2 h.

thickness catalyst before calcination. This demonstrated that the thinner the SiO_2 shell thickness, the easier it is for Ni to be oxidized. This probably is due to the largest Ni exposure for the 3.3 nm thickness catalyst (see Table 1).

To get the physical structure stability information before and after 20 h of the DRM reaction, argon physisorption analysis at 87 K for Ni@SiO_2 with 8.6 nm shell thickness and Ni−yolk@Ni@SiO_2 with 11.2 and 15.1 nm shell thickness catalysts was performed. This analysis was not performed on the 3.3 and 5.7 nm shell thickness Ni@SiO_2 catalyst because their core shell structures collapsed with large amounts of carbon deposition, as indicated in Figures 4 and 5. As summarized in Table 2, before the reaction, the specific surface area decreases by 21% and 38%, respectively, when the shell thickness increases from 8.6 to 11.2 nm and from 11.2 to 15.1 nm. As for total pore volume, there is a slight increase from 0.42 to 0.49 $cm^3 \cdot g^{-1}$ followed by a sharp decrease (by 78%) when the thickness increases to 15.1 nm.

Table 2. Physical Properties of Ni@SiO_2 and Ni−yolk@Ni@SiO_2 with Different Shell Thicknesses before and after Reaction

	specific Surface area ($m^2 \cdot g^{-1}$)		total pore volume ($cm^3 \cdot g^{-1}$)		NLDFT pore size (nm)	
shell thickness (nm)	before[a]	after[b]	before[a]	after[b]	before[a]	after[b]
8.6	77	70	0.42	0.40	1.58	1.51
11.2	61	59	0.49	0.45	1.71	1.71
15.1	38	29	0.11	0.07	1.54	1.37

[a]The values are obtained over the catalysts after 2 h of calcination in air . [b]The values are obtained over the catalysts after 20 h of the DRM reaction at 800 °C.

The decrease of the specific surface area and total pore volume with the increase of shell thickness can be attributed to the increase of the silica shell density. On the basis of the synthesis process of core shell catalysts, thicker silica shell thickness was achieved by a greater amount of TEOS and longer reaction time. Therefore, the greater extent of hydrolysis and condensation of TEOS results in a more dense silica shell. Upon calcination, a greater extent of dehydroxylation occurred for thicker shells containing more hydroxyl groups. In addition, the increasing density of silica shell with increases in shell thickness also can be confirmed from the increasing of micropore percentage, as shall be discussed later. The small increase in the total pore volume is due to the formation of yolk shell structure, leading to the increase of the void space between Ni and silica.

After reaction, the specific area and total pore volume for the 8.6 nm thickness Ni@SiO_2 and 11.2 nm thickness Ni−yolk@Ni@SiO_2 decreased slightly. From Figure 4b,c, the void space between Ni core and silica shell can still be seen after reaction. However, they significantly decreased for the 15.1 nm thickness Ni−yolk@Ni@SiO_2. This can be ascribed to the occurrence of the severe reverse water gas shift reaction, leading to cross-linking between Ni−yolk@Ni@SiO_2 particles, as indicated in Figure 4e.

As for the pore size distribution (see Figure 7), no obvious change (less than 8%) for pore size was observed when shell thickness increased. This is because the same Igepal CO-630 surfactant was used to generate pores among these catalysts. However, the composition of the pore structures changed. When the shell thickness increased from 8.6 to 15.1 nm, the percentage of micropores increased from 27% (8.6 nm thickness), 34% (11.2 nm thickness) to 41% (15.1 nm thickness), respectively. The percentage of the 5.2 nm pore decreases with the increase of shell thickness and nearly becomes zero when the thickness increases to 15.1 nm. This indicates the increase of shell density with increases in shell thickness. After reaction, the pore size also did not change much for the 8.6 nm Ni@SiO_2 and 11.2 nm thickness Ni−yolk@Ni@SiO_2, which is similar to the specific area and total pore volume indicating the structural stability of these two catalysts. Whereas, for 15.1 nm thickness Ni−yolk@Ni@SiO_2, it decreased by 11%, from 1.54 to 1.37 nm. In addition, after reaction, only micropores were left. This also can be ascribed to the formation of silica gel networks after reaction as discussed above.

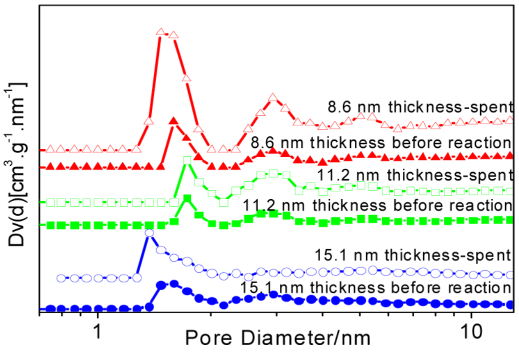

Figure 7. Pore size distribution of Ni@SiO_2 and Ni−yolk@Ni@SiO_2 with different shell thickness before and after reaction.

2.5. Surface Ni Species and Reducibility Properties.

Figure 8 demonstrates the chemical state of surface Ni species. As presented in Figure 8, the Ni $2p_{3/2}$ XPS spectra exhibit a main peak that shifts to higher BE values from 856.3 to 856.9 eV and becomes broader with the increase in shell thickness. This illustrates the increase in the interaction between the Ni core and silica shell and the formation of new Ni species when the shell thickness is greater than 8.6 nm. Despite that the interface between NiO surfaces and silica in these catalysts are all the same because NiO were all fully covered by silica, the strength of the chemical bond formed at the interface is

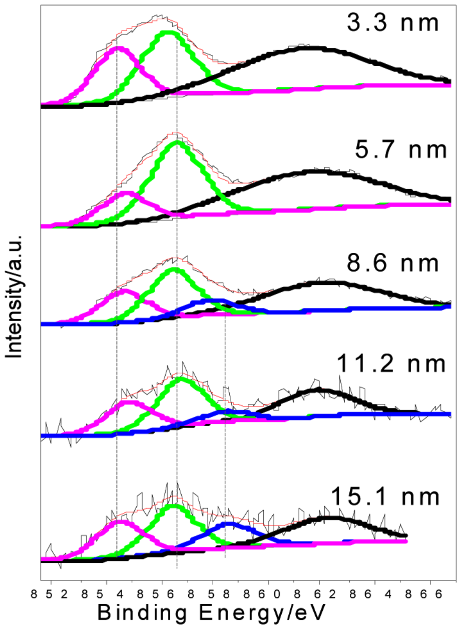

Figure 8. Ni $2p_{3/2}$ photoelectron spectrum of Ni@SiO_2 and Ni−yolk@Ni@SiO_2 with different shell thicknesses.

different, resulting in different Ni core and silica shell interactions. The different chemical bond strengths can be attributed to different extents of the reaction between NiO and silica, leading to the formation of different kinds of surface nickel silicate species. In addition, it can be seen from Figure 8 that the intensity of Ni$2p_{3/2}$ decreases with the increase of shell thickness. This can be attributed to the increase in the relative intensity ratio between surface Ni and Si with the increase of surface Ni concentration and the decrease of shell thickness (Figure S6, Supporting Information). This is in accordance with the results reported by Kirumakki that the XPS intensity of Ni$2p_{3/2}$ increases with increases in Ni loading.[53]

Particularly, peaks centered at around 854.7, 856.6 and 858.9 eV can be assigned to NiO, 1:1 nickel phyllosilicate ($Ni_3(Si_2O_5)(OH)_4$) and 2:1 nickel phyllosilicate ($Ni_3(Si_2O_5)_2(OH)_2$), respectively. The assignment of 854.7 eV to NiO is plausible with the support of its O 1s BE value of 530.3 eV (Table S2, Supporting Information). In addition, the BE value of the satellite peak is 6 eV higher than Ni $2P_{3/2}$, which provides additional evidence for this assignment. This is consistent with the previous studies by T. Lehmann[52] and G. Wendt et al.[54] The rather high BE value of 858.9 eV can be ascribed to 2:1 nickel phyllosilicate because it has the highest BE value among the silicate species that have been reported.[52,55]

It is difficult to solely distinguish 1:1 nickel phyllosilicate from other silicates such as Ni_2SiO_4 and $NiSiO_3$ from the BE value because they are all between 855.6 and 856.9 eV.[52] However, another indicator, ΔE_{Ni-Si}, which is the binding energy difference between Ni $2p_{3/2}$ and Si 2p, has been used by T. Lehmann[52] and Coenen[56] et al. to confirm its formation. As revealed in Table 3, ΔE_{Ni-Si} values are well matched with the valve of 1:1 phyllosilicates (752.8 and 753.8 eV) reported by T. Lehmann.[52] In addition, the O 1s BE value between 531.1 and 532.2 eV (Table S2, Supporting Information) is also consistent with the studies for 1:1 phyllosilicates by J. C. Vedrine.[57] All these XPS results confirmed the presence of 1:1 nickel phyllosilicate. Even though it is reported that 1:1 nickel phyllosilicates will decompose between 600 and 830 °C,[52] high crystallinity 1:1 nickel phyllosilicate may be preserved. J. Y. Carriat also reported the strong influence of synthesis temperature to the crystallinity of 1:1 nickel phyllosilicate.[58] Further, no obvious sintering of the 3.3 nm shell thickness catalyst after 20 h of calcination at 800 °C (see Figure S5a, Supporting Information) showed the persistence of high crystalline 1:1 nickel phyllosilicate. Otherwise, NiO from Ni core surface will sinter with the NiO decomposed from 1:1 nickel phyllosilicate, forming bigger particles. Because no obvious nickel phyllosilicate phases were detected by XRD (Figure 6), their presence in the bulk Ni@SiO_2 catalysts are in small quantity compared with NiO. The presence of different crystallinity 1:1 nickel phyllosilicates can be confirmed from the broad reduction peak from 500 to 700 °C (see Figure 9), as discussed below.

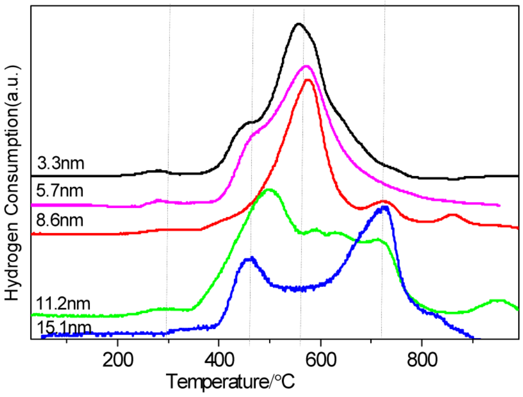

Figure 9. TPR-H_2 profiles of Ni@SiO_2 and Ni−yolk@Ni@SiO_2 with different shell thicknesses.

Table 3. Ni $2p_{3/2}$ Binding Energy and Surface Ni Species Proportion of Ni@SiO_2 and Ni−yolk@Ni@SiO_2 with Different Shell Thicknesses

		NiO		1:1 phyllosilicates			2:1 phyllosilicates		
thickness (nm)	Ni/Si ratio[a]	Ni $2p_{3/2}$ (eV)	propor tion (%)	Ni $2p_{3/2}$ (eV)	propor tion (%)	ΔE_{Ni-Si}[b] (eV)	Ni $2p_{3/2}$ (eV)	ΔE_{Ni-Si}[b] (eV)	propor tion (%)
3.3	3.94	854.5	48.7	856.3	51.3	754.0			
5.7	0.84	854.8	31.9	856.7	68.1	754.0			
8.6	0.51	854.7	34.2	856.6	57.5	753.6	858.3	754.8	8.3
11.2	0.25	854.9	36.1	856.9	56.5	753.1	858.9	755.1	7.4
15.1	0.19	854.5	35.2	856.6	45.7	752.9	858.9	755.2	19.1

[a] Determind from ICP analysis. [b] ΔE_{Ni-Si} = Ni $2p_{3/2}$ − Si 2p

By deconvolution, the areas under the curve of each peak in Figure 4 were used to estimate the relative surface proportion of each nickel species (Table 3). As indicated in Table 3, the fraction of NiO decreased greatly from 48.7% to 31.9% when the shell thickness increased from 3.3 to 5.7 nm. It has been reported that the Ni/Si ratio determines the nature of nickel phyllosilicate. When the Ni/Si ratio is higher than 1.5, pure 1:1 nickel phyllosilicate will be formed.[59] White also demonstrated the formation of 1:1 nickel phyllosilicate nanotubes with Ni/Si ratio between 1 and 3.[60] 2:1 nickel phyllosilicate will be obtained when Ni/Si ratio is between 0.5 and 0.75.[59]

On the basis of this knowledge, it is easier to understand that 1:1 nickel phyllosilicates are favorable to form for catalysts with shell thickness of 3.3 and 5.7 nm because their Ni/Si ratios are large enough. The decrease of the NiO phase with the increase in shell thickness from 3.3 to 5.7 nm might be due to the more extent of reaction between NiO and silica caused by much closer contact of NiO and silica as evidenced by the decrease of specific area and total pore volume in Table 2. In other words, the stronger interaction between nickel and silica for the 5.7 nm shell thickness lead to more extent of reaction and thereby the increase of the 1:1 nickel phyllosilicate proportion, as indicated in Table 3.

With further increases in shell thickness from 5.7 to 11.2 nm, the proportion of NiO gradually increases. This can be attributed to the fact that their Ni/Si ratio is equal to or less than 0.5, which is favorable for the formation of 2:1 nickel phyllosilicate. Therefore, 1:1 nickel phyllosilicate will decompose to NiO and transform into 2:1 nickel phyllosilicate, resulting in an increase of their proportion. It is noted that the proportion of 2:1 nickel phyllosilicate for the 11.2 nm shell thickness catalyst decreased a bit compared with that of 8.6 nm shell thickness. This is probably due to the slight decrease in the nickel and silica interface caused by the formation of the yolk shell structure as discussed above, leading to the slight drop of reaction extent between NiO and silica. Whereas when the shell thickness increased to 15.1 nm, even though the yolk shell structure still exists, the effect brought by the sharp decrease of its specific area and total pore volume results in a stronger interaction between NiO and silica compared with 11.2 nm shell thickness, causing the sharp increase of 2:1 nickel phyllosilicate.

The XPS analysis for nickel species correlates well with their reducibility examined by TPR-H_2, as shown in Figure 9. On the whole, the reduction peaks for 3.3 and 5.7 nm shell thickness were below 590 °C. When shell thickness is greater than 8.6 nm, reduction peaks higher than 700 °C appeared and their relative intensities became higher compared with the reduction peaks below 700 °C, indicating the increase of interaction between Ni and silica with the increase of shell thickness. This is consistent with the appearance of 2:1 nickel phyllosilicate new species when shell thickness is greater than 8.6 nm, as discussed above. In addition, the reduction peaks around 580 °C became broader when shell thickness was greater than 8.6 nm, especially for the 11.2 nm thickness Ni−yolk@Ni@SiO_2, indicating the presence of different crystalline 1:1 nickel phyllosilicate species, as discussed below. Upon reduction, small Ni particles around the Ni core within the silica shell will be formed (see Figure 4c,d,f).

Specifically, the reduction peaks centered at around 300 and 460 °C can be attributed to NiO species with different interaction with silica shell.[61] Broad peaks between 580 and 700 °C may be due to NiO decomposed from ill crystallized 1:1 nickel phyllosilicate and a small amount of highly crystalline 1:1 nickel phyllosilicate, as indicated by XPS analysis. It is reported that the reduction temperature for NiO decomposed from 1:1 phyllosilicate and for 1:1 nickel phyllosilicate itself is around 540 °C[61] and 450−650 °C, respectively.[52] Higher crystallinity of 1:1 nickel phyllosilicate will lead to higher reduction temperature.[62] Therefore, based on these phenomena, the above assignment is reasonable. The peaks above 700 °C can be assigned to 2:1 nickel phyllosilicate based on its reported reduction temperature between 690 and 760 °C.[52]

2.6. Activity and Stability Discussion. The above characterizations of both fresh catalysts and spent catalysts provide good indications for the effect of silica shell thickness on catalyst structure and catalytic activity and stability. The structural instability of the 3.3 nm shell thickness Ni@SiO_2 lead to severe Ni sintering and severe carbon formation, which resulted in its low specific activity of CH_4 and CO_2. Its structural instability is caused by the weak interaction between the Ni core and the silica shell which is more easily broken by the deposited carbon species. With the increased Ni-SiO_2 interaction, the core shell structural stability for 5.7 nm shell thickness Ni@SiO_2 improved, resulting in less Ni sintering and carbon deposition. The formation of nickel phyllosilicate species in the interface of the Ni core and the silica shell further improved the structural stability of Ni−yolk@Ni@SiO_2 when the shell thickness was greater than 8.6 nm, leading to no Ni sintering and negligible carbon deposition. In addition, small satellite Ni nanoparticles around the Ni core within the silica shell formed from decomposition of nickel phyllosilicate species upon reduction improved their catalytic activity. Further, the formation of yolk shell structures for 11.2 nm shell thickness Ni−yolk@Ni@SiO_2 contributed to its highest catalytic activity and TOF value of 79 s^{-1}. It has been reported by Chak-Tong Au's group that the void space between the Ni core and the silica shell provides a uniform reaction environment, the so-called confinement effect, and increases the adsorption ability of Ni for reactant gases, resulting in good catalytic activity.[29] The significant decrease of specific area and total pore volume, as well as the considerable low Ni exposure, lead to the lowest catalytic activity for 15.1 nm shell thickness Ni−yolk@Ni@SiO_2.

The changes in the H_2/CO ratio with increased shell thickness reflect the predominance of different adverse reactions for different shell thickness catalysts. For 3.3 nm shell thickness catalyst, severe Ni sintering lead to the predominance of CH_4 decomposition reaction, which is favored for catalysts with large Ni particle sizes.[63] This resulted in the relative high H_2/CO ratio. Less Ni sintering for 5.7 nm shell thickness catalyst lead to suppression of CH_4 decomposition reaction, which is in accordance with its alleviated carbon deposition and thereby the drop of H_2/CO ratio. When shell thickness is greater than 8.6 nm, the reverse water gas shit side reaction became predominant compared with other side reactions, resulting in the slight drop of the H_2/CO ratio for 11.2 nm shell thickness catalyst and the extremely low H_2/CO ratio for 15.1 nm shell thickness Ni−yolk@Ni@SiO_2. This can be due to the fact that no Ni sintering happened to the catalysts with shell thickness greater than 8.6 nm because of the strong Ni−SiO_2 interaction as well as the formation of nickel phyllosilicate species. It is reported that CO and CO_2 machination reactions and the CH_4 decomposition reaction are all favored on bulk Ni particles.[63,64] In addition, it is revealed that the reverse water gas shift reaction is predominant for both 1:1 and 2:1 nickel phyllosilicates for DRM reactions above 600 °C.[64]

3. CONCLUSIONS

A yolk−satellite−shell structured Ni−yolk@Ni@SiO_2 nanocomposite was for the first time synthesized by varying the silica shell thickness of Ni@SiO_2 nanoparticles. The effect of silica shell thickness to the structure as well as catalytic performance for CO_2 reforming of methane reaction was for the first time discussed. It was found that the formation of Ni−yolk@Ni@SiO_2 nanocomposite was highly shell thickness dependent thereby influencing the catalytic activity and carbon resistant ability. Compared with Ni@SiO_2, Ni−yolk@Ni@SiO_2 with 11.2 nm shell thickness showed superb catalytic activity of 90% CH_4 conversion and 95% CO_2 conversion for 90 h with negligible carbon being detected by TGA. The formation of nickel phyllosilicate species due to the strong interaction between Ni core and silica shell contributed to the improved catalytic performance compared with Ni@SiO_2. Small satellite Ni particles within the silica shell improved the catalytic activity. The evolution of core shell structure to yolk shell structure upon calcination further increased its catalytic activity due to the confinement effect. The newly found phenomenon for yolk shell structure nanocomposites formation provides a promising and facile method to synthesize other metal@SiO_2 yolk shell nanocomposites without using post treatment processes such as template removal and strong acid etching. In addition, the specific surface area of yolk shell structure materials can be further improved through addition of pore swelling agents to improve the performance of solar energy transfer and sustainable energy production.

4. EXPERIMENTAL SECTION

4.1. Synthesis of Ni−yolk@Ni@SiO_2 Nanocomposites. First, Ni@SiO_2 core shell nanoparticles with different shell thickness were synthesized. Typically, 2 g Nickel(II) acetylacetonate was predispersed into oleylamine (70%) and degassed under N_2 before transferring to a preheated 240 °C oil bath. Then trioctylphosphine (90%) was added into the mixture and kept at 230 °C for 2 h. After that, Ni nanoparticles were separated and added into a microemulsion with the composition of 300 mL cyclohexane, 20 mL Igepal CO-630 and ammonia. Corresponding amount of TEOS was dropwise added by a syringe pump (see Table S1). Ni@SiO_2 nanoparticles with different shell thickness were obtained by separating and washing twice with ethanol.

Second, after drying in air at room temperature, Ni@SiO_2 nanoparticles were calcined at 800 °C for 2 h. Ni−yolk@Ni@SiO_2 nanocomposites were formed with the silica shell thickness of 11.2 and 15.1 nm.

4.2. Physical Characterization. The morphology of Ni nanoparticles, Ni@SiO_2 and Ni−yolk@Ni@SiO_2 nanocomposite were characterized by TEM and HRTEM. Samples were prepared by dropping Ni in cyclohexane, Ni@SiO_2 and Ni−yolk@Ni@SiO_2 in ethanol, respectively, on a copper grid. The surface areas and pore size distribution of the catalysts were determined by a NOVA 2200 system (Quantachrome). The surface area was calculated using the Brunauer−Emmett−Teller method using the adsorption data. The pore size distribution was obtained from the adsorption isotherm by the NLDFT method. Shimadzu XRD-6000 diffractometer using Cu Kα radiation (40 kV, 30 mA) was employed to determine the characteristic peak of Ni nanoparticles and silica phase. Nickel loading of Ni@SiO_2 catalyst was measured with Agilent ICP-MS 7700 series. 0.01 g samples were dissloved by a mixture of 0.05 mL HF (48%) and 2 mL HNO_3 (60%) aided by ultrasonic treatment at 60 °C. Thermogravimetric analyzer (Shimadzu DTG-60) in static air was employed to determine the amount of carbon deposited on the catalyst after the DRM reaction. H_2 chemisorption and TPR-H_2 was performed on Quantachrome Chem-BET-3000. H_2 pulse titration was conducted after reduction by pure H_2 at 800 °C for 1h followed by cooling down to 30 °C under the purging of N_2. XPS with concentric hemispherical analyzer and Al Kα gun X-ray source was used to characterize the surface Ni species for calcined catalysts.

4.3. Catalyst Evaluation. DRM reaction experiments were conducted in a quartz tube reactor with an inner diameter of 4 mm under atmospheric pressure. Before reaction, the calcined catalyst was reduced at 800 °C for 1 h followed by N_2 purging and introduction of CO_2 and CH_4. The composition of the product gases was analyzed with an on-line gas chromatograph (HP 6890) equipped with a thermal conductivity detector.

■ ASSOCIATED CONTENT

Ⓢ Supporting Information

TEM image, XRD pattern and size distribution of Ni nanoparticles; particle size distribution of Ni@SiO2 and Ni−yolk@Ni@SiO2 nanocomposites with different shell thickness determined from TEM images; mass transfer limitation tests using 3.3 nm shell thickness Ni@SiO2 and 11.2 nm shell thickness Ni−yolk@Ni@SiO2 nanocomposite as examples. Error bar stands for data tested; EDX mapping for Ni@SiO2 spent catalysts with 3.3 nm silica shell thickness; TEM images for catalysts after calcination at 800 °C for 20 h in static air with 3.3 nm shell thickness Ni@SiO2 and 15.1 nm shell thickness Ni−yolk@Ni@SiO2 nanocomposite; relative intensity ratio I_{Ni}/I_{Si} against surface Ni concentration of catalysts with different shell thickness; synthesis parameters, Ni and Si loading determined from ICP analysis for catalysts with different shell thickness; O 1s binding energy for Ni species of catalysts with different shell thickness. This material is available free of charge via the Internet at http://pubs.acs.org.

■ AUTHOR INFORMATION

Corresponding Author

*S. Kawi. E-mail: chekawis@nus.edu.sg.

Notes

The authors declare no competing financial interest.

■ ACKNOWLEDGMENTS

The authors gratefully thank the National University of Singapore and A*STAR (A*STAR SERC 092-138-0022, RP No. 279-000-292-305), NEA (NEA-ETRP 1002114, RP No. 279-000-333-490), and NRF (NRF-POC 001-055) for generously supporting this work. Li Ziwei thanks Prof K. Hidajat for his suggestions and the China Scholarship Council for supporting his Ph.D. work.

■ REFERENCES

(1) Wang, N.; Shen, K.; Huang, L.; Yu, X.; Qian, W.; Chu, W. *ACS Catal.* **2013**, *3*, 1638−1651.

(2) Edwards, J. H.; Maitra, A. M. *Fuel Process. Technol.* **1995**, *42*, 269−289.

(3) Wörner, A.; Tamme, R. *Catal. Today* **1998**, *46*, 165−174.

(4) Kodama, T. *Prog. Energ. Combust.* **2003**, *29*, 567−597.

(5) Han, W.; Jin, H.; Lin, R. *J. Sol. Energ-T ASME* **2011**, 133.

(6) Max Lu, G. Q.; Wang, S. *J. Dev. Chem. Eng. Miner. Process* **1999**, *7*, 443−462.

(7) Liu, C. J.; Ye, J.; Jiang, J.; Pan, Y. *ChemCatChem* **2011**, *3*, 529−541.

(8) García-Diéguez, M.; Pieta, I. S.; Herrera, M. C.; Larrubia, M. A.; Alemany, L. J. *J. Catal.* **2010**, *270*, 136−145.

(9) Huang, B.; Li, X.; Ji, S.; Lang, B.; Habimana, F.; Li, C. *J. Nat. Gas Chem.* **2008**, *17*, 225−231.

(10) Li, Y.; Zhang, B.; Xie, X.; Liu, J.; Xu, Y.; Shen, W. *J. Catal.* **2006**, *238*, 412−424.

(11) Pan, Y.-x.; Liu, C.-j.; Wiltowski, T. S.; Ge, Q. *Catal. Today* **2009**, *147*, 68−76.

(12) Roh, H.-S.; Jun, K.-W. *Catal. Surv. Asia* **2008**, *12*, 239−252.

(13) Corthals, S.; Van Nederkassel, J.; Geboers, J.; De Winne, H.; Van Noyen, J.; Moens, B.; Sels, B.; Jacobs, P. *Catal. Today* **2008**, *138*, 28−32.

(14) Daza, C. E.; Kiennemann, A.; Moreno, S.; Molina, R. *Appl. Catal., A* **2009**, *364*, 65−74.

(15) Alexeev, O. S.; Gates, B. C. *Ind. Eng. Chem. Res.* **2002**, *42*, 1571−1587.

(16) Li, D.; Nakagawa, Y.; Tomishige, K. *Appl. Catal., A* **2011**, *408*, 1−24.

(17) Sutthiumporn, K.; Kawi, S. *Int. J. Hydrogen Energy* **2011**, *36*, 14435−14446.

(18) Sutthiumporn, K.; Maneerung, T.; Kathiraser, Y.; Kawi, S. *Int. J. Hydrogen Energy* **2012**, *37*, 11195−11207.

(19) Yung, M. M.; Kuhn, J. N. *Langmuir* **2010**, *26*, 16589−16594.

(20) Kambolis, A.; Matralis, H.; Trovarelli, A.; Papadopoulou, C. *Appl. Catal., A* **2010**, *377*, 16−26.

(21) Hua, W.; Jin, L.; He, X.; Liu, J.; Hu, H. *Catal. Commun.* **2010**, *11*, 968−972.

(22) Cargnello, M.; Doan-Nguyen, V. V. T.; Gordon, T. R.; Diaz, R. E.; Stach, E. A.; Gorte, R. J.; Fornasiero, P.; Murray, C. B. *Science* **2013**, *341*, 771−773.

(23) Adijanto, L.; Sampath, A.; Yu, A. S.; Cargnello, M.; Fornasiero, P.; Gorte, R. J.; Vohs, J. M. *ACS Catal.* **2013**, *3*, 1801−1809.

(24) Chen, C.; Cao, J.; Cargnello, M.; Fornasiero, P.; Gorte, R. J. *J. Catal.* **2013**, *306*, 109−115.

(25) Pérez-Lorenzo, M.; Vaz, B.; Salgueiriño, V.; Correa-Duarte, M. A. *Chem.—Eur. J.* **2013**, *19*, 12196−12211.

(26) Li, L.; He, S.; Song, Y.; Zhao, J.; Ji, W.; Au, C.-T. *J. Catal.* **2012**, *288*, 54−64.

(27) Li, L.; Lu, P.; Yao, Y.; Ji, W. *Catal. Commun.* **2012**, *26*, 72−77.

(28) Li, Y.; Zhang, X. L.; Qiu, R.; Qiao, R.; Kang, Y. S. *J. Phys. Chem. C* **2007**, *111*, 10747−10750.

(29) Yao, L. H.; Li, Y. X.; Zhao, J.; Ji, W. J.; Au, C. T. *Catal. Today* **2010**, *158*, 401−408.

(30) Cargnello, M.; Delgado Jaén, J. J.; Hernández Garrido, J. C.; Bakhmutsky, K.; Montini, T.; Calvino Gámez, J. J.; Gorte, R. J.; Fornasiero, P. *Science* **2012**, *337*, 713−717.

(31) Park, M.; Seo, S.; Lee, S. J.; Jung, J. H. *Analyst* **2010**, *135*, 2802−2805.

(32) Tadić, M.; Panjan, M.; Marković, D. *Mater. Lett.* **2010**, *64*, 2129−2131.

(33) Peng, K.; Zhou, L.; Hu, A.; Tang, Y.; Li, D. *Mater. Chem. Phys.* **2008**, *111*, 34−37.

(34) Takenaka, S.; Umebayashi, H.; Tanabe, E.; Matsune, H.; Kishida, M. *J. Catal.* **2007**, *245*, 392−400.

(35) Park, J. C.; Bang, J. U.; Lee, J.; Ko, C. H.; Song, H. *J. Mater. Chem.* **2010**, *20*, 1239.

(36) Takenaka, S.; Orita, Y.; Umebayashi, H.; Matsune, H.; Kishida, M. *Appl. Catal., A* **2008**, *351*, 189−194.

(37) Park, J. C.; Lee, H. J.; Kim, J. Y.; Park, K. H.; Song, H. *J. Phys. Chem. C* **2010**, *114*, 6381−6388.

(38) Jiang, Z.; Xie, J.; Jiang, D.; Jing, J.; Qin, H. *CrystEngComm* **2012**, *14*, 4601.

(39) Joo, S. H.; Park, J. Y.; Tsung, C.-K.; Yamada, Y.; Yang, P.; Somorjai, G. A. *Nat. Mater.* **2009**, *8*, 126−131.

(40) Forman, A. J.; Park, J. N.; Tang, W.; Hu, Y. S.; Stucky, G. D.; McFarland, E. W. *ChemCatChem* **2010**, *2*, 1318−1324.

(41) Park, J. N.; Forman, A. J.; Tang, W.; Cheng, J.; Hu, Y. S.; Lin, H.; McFarland, E. W. *Small* **2008**, *4*, 1694−1697.

(42) Ammar, M.; Mazaleyrat, F.; Bonnet, J. P.; Audebert, P.; Brosseau, A.; Wang, G.; Champion, Y. *Nanotechnology* **2007**, *18*, 285606.

(43) Park, J. C.; Song, H. *Nano Res.* **2011**, *4*, 33−49.

(44) Lee, J.; Park, J. C.; Bang, J. U.; Song, H. *Chem. Mater.* **2008**, *20*, 5839−5844.

(45) Park, S. J.; Kim, Y. J.; Park, S. J. *Langmuir* **2008**, *24*, 12134−12137.

(46) Kapteijn, F.; Moulijn, J. A. *Handbook of Heterogeneous Catalysis*; Wiley-VCH Verlag GmbH & Co. KGaA: Weinheim, Germany, 2008.

(47) Kang, K.-M.; Kim, H.-W.; Shim, I.-W.; Kwak, H.-Y. *Fuel Process. Technol.* **2011**, *92*, 1236−1243.

(48) Bradford, M. C. J.; Vannice, M. A. *Catal. Rev.* **1999**, *41*, 1−42.

(49) Vigil, G.; Xu, Z.; Steinberg, S.; Israelachvili, J. *J. Colloid Interface Sci.* **1994**, *165*, 367−385.

(50) Roh, T. W.; Lee, M. H.; Mun, J. H.; Yeo, S. H.; Kim, M. T.; Lee, S. H.; Huh, J. S. *J. Ceram. Process Res.* **2012**, *13*, 797−800.

(51) Chen, Y.-g.; Tomishige, K.; Yokoyama, K.; Fujimoto, K. *Appl. Catal., A* **1997**, *165*, 335−347.

(52) Lehmann, T.; Wolff, T.; Hamel, C.; Veit, P.; Garke, B.; Seidel-Morgenstern, A. *Microporous Mesoporous Mater.* **2012**, *151*, 113−125.

(53) Kirumakki, S. R.; Shpeizer, B. G.; Sagar, G. V.; Chary, K. V. R.; Clearfield, A. *J. Catal.* **2006**, *242*, 319−331.

(54) Wilson, M. F.; Mainwaring, P. R.; Brown, J. R.; Kriz, J. F. *Appl. Catal.* **1988**, *41*, 177−198.

(55) Wendt, G.; Hentschel, D.; Finster, J.; Schöllner, R.; Hanafi, S.; Mikhail, R. S. *J. Chem. Soc., Faraday Trans. 1* **1983**, *79*, 2013−2025.

(56) Coenen, J. W. E. *Appl. Catal.* **1991**, *75*, 193−223.

(57) Vedrine, J. C.; Hollinger, G.; Duc, T. M. *J. Phys. Chem.* **1978**, *82*, 1515−1520.

(58) Carriat, J. Y.; Che, M.; Kermarec, M.; Decarreau, A. *Catal. Lett.* **1994**, *25*, 127−140.

(59) Burattin, P.; Che, M.; Louis, C. *J. Phys. Chem. B* **1998**, *102*, 2722−2732.

(60) White, R. D.; Bavykin, D. V.; Walsh, F. C. *J. Mater. Chem. A* **2013**, *1*, 548−556.

(61) Pan, Y.-X.; Liu, C.-J.; Shi, P. *J. Power Sources* **2008**, *176*, 46−53.

(62) Burattin, P.; Che, M.; Louis, C. *J. Phys. Chem. B* **1997**, *101*, 7060−7074.

(63) Chen, D.; Christensen, K.; Ochoafernandez, E.; Yu, Z.; Totdal, B.; Latorre, N.; Monzon, A.; Holmen, A. *J. Catal.* **2005**, *229*, 82−96.

(64) Sivaiah, M. V.; Petit, S.; Beaufort, M. F.; Eyidi, D.; Barrault, J.; Batiot-Dupeyrat, C.; Valange, S. *Microporous Mesoporous Mater.* **2011**, *140*, 69−80.